Fluid Migration Characterization of Full-Scale Annulus Cement Sections Using Pressure-Pulse-Decay Measurements

Hans Joakim Skadsem

Department of Energy and Petroleum Engineering,
University of Stavanger,
P. O. Box 8600,
4036 Stavanger, Norway;
NORCE Norwegian Research Centre AS,
P. O. Box 8046,
4068 Stavanger, Norway
e-mail: hans.j.skadsem@uis.no

Fluid migration behind casings is a well integrity problem that can result in sustained casing pressure, undetected leaks to the environment, and potentially very challenging remediation attempts. Understanding the geometric dimensions and extent of annular migration paths is important for diagnosing and effectively treating fluid migration and sustained casing pressure problems in wells. In this study, permeability and micro-annuli sizes in two full-scale cemented annulus test sections are measured using transient pressure-pulse-decay and steady-state seepage measurements. One of the studied sections is a cemented 9 5/8-in. and 13 3/8-in. casing section from a 30 years old Norwegian North Sea production well. A model for predicting the transient pressure decay in annular sections with non-uniform permeability is presented and the permeabilities of the two sections are determined by fitting the transient model to pressure measurements at either side of the test sections and at selected axial positions. For both sections, measured micro-annulus sizes are within the range of effective wellbore permeabilities based on sustained casing pressure records and previous vertical interference tests from other wells. The test sections display measurable axial permeability variations with the bottom part of these vertical sections having the lower permeability. For the retrieved casing section, the axial permeability variation occurs close to the middle of the test section and is attributed to the top-of-cement. Increasing internal casing pressure is found to slightly reduce the equivalent micro-annulus size, indicative of fracture-like response of the migration paths. Using two independent test protocols, we have measured effective permeabilities as well as local permeability variations in full-scale test sections and found consistent results. The study suggests that the transient test procedure can be used to more effectively characterize low-permeable annular cement where it is otherwise time-consuming or difficult to establish steady-state flow conditions. [DOI: 10.1115/1.4052184]

Keywords: deep-water petroleum, petroleum engineering, petroleum wells-drilling/production/construction

1 Introduction

The cement behind casings is an important structural barrier element in wells for oil and gas production that should ensure zonal isolation along the annulus and provide mechanical support for the casing. The cement is usually placed behind the casing or liner by pumping a sequence of fluids, including washing fluids, spacer fluids, and the cement slurry, down the well inside the casing. The fluids flow into the annulus and up toward the surface from the bottom of the casing, displacing the original drilling fluid from the annular space behind the casing.

Once hardened, a main function of the well cement is to prevent the uncontrolled flow of fluids behind the casing. As discussed by Bois et al. [1] and Patel and Salehi [2], the set cement is subjected to mechanical and thermal loads that can comprise annular zonal isolation. A consequence can be fluid migration problems leading to sustained casing pressure or surface casing vent flows at the surface. Brufatto et al. reported in 2003 that out of approximately 15,500 producing, shut-in and temporarily abandoned wells on the outer continental shelf of the Gulf of Mexico (period 1973–2003), 43% exhibited sustained casing pressure (SCP) on at least one casing annulus [3]. A recent overview of world-wide statistics related to barrier and well integrity failures is provided by Davies et al. [4].

While cements that are cured under controlled and undisturbed conditions exhibit low bulk permeabilities in the microdarcy range [5], effective permeabilities in wells with sustained casing pressure have been found to be several orders of magnitude greater due to various flaws such as fractures or poor bond between casing or formation and the cement [6–9]. Indeed, the effective wellbore permeability of cemented annuli can be very different from the permeability of bulk cement due to flow along micro-annuli or fractures.

Sustained casing pressure records, vertical interference tests, cement logs, and operational data are important sources of information about the actual wellbore permeability. Gasda et al. [10] reported wellbore permeability measurements from vertical interference tests and compared the permeabilities to cement bulk permeabilities measured on cored material from the side wall. While the cement cores exhibited permeabilities of the order of microdarcy to hundreds of microdarcy, the corresponding wellbore permeabilities were at least 2 orders of magnitude greater than the bulk permeability [10]. Working with sustained casing pressure buildup data from 238 wells, Checkai et al. determined the effective wellbore permeabilities to be in the range from 1 microdarcy up to 1 darcy [11]. Assuming the leakage occurs outside a 9 5/8-in. production casing, a 1 darcy permeability corresponds to a $70\,\mu m$ micro-annulus gap between the annulus cement and the outer 13 3/8-in. casing [9]. Similar effective wellbore permeabilities have also

been reported by Crow et al. [12] and Kang et al. [13]. When combined with a model for fluid migration along the wellbore, sustained casing pressure records can be used to assess properties of the migration paths and leakage rates [14].

A new source of information concerning effective wellbore permeabilities is two *sandwich sections* consisting of production casing (244.5 mm or 9 5/8-in. outer diameter) and intermediate casing (339.7 mm or 13 3/8-in. outer diameter) with the annular cement sandwiched in-between that were cut and retrieved to surface as part of a recent abandonment operation in a Norwegian North Sea well. The sections were cut in approximately 10 m lengths from the well interval between 119 m and 263 m vertical depth as part of the surface plugging operation. The well was originally constructed and cemented in 1985 and experienced sustained casing pressure during production. The well was permanently abandoned in 2018, and two of the retrieved sections were saved for surface re-logging and characterization. The surface re-logging confirmed the log results acquired in the well prior to cutting and retrieving the sections, namely, the existence of poor-to-moderate cement bond to the inner casing and indications of gas on the ultrasonic cement log [15,16]. An initial comparison between the cement logs and seepage records showed good, qualitative agreement [15,16]. In this paper, I expand on the above by measuring wellbore permeability, or the equivalent micro-annulus gap size, in one of the two sandwich sections mentioned above, and in another, yard-cemented full-scale annulus test section, using two different techniques, namely, the transient pressure-pulse-decay method and steady-state seepage measurements.

In laboratory tests, effective annular permeability or equivalent effective micro-annulus of annular cement is often inferred from measurements of volumetric flowrate as function of applied pressure difference across the test sample. An alternative measurement technique to the steady-state seepage measurements is the transient pressure-pulse-decay method where the permeability is inferred from the pressure propagation through the sample. The sample to be tested is connected to an upstream and a downstream fluid reservoir, with sample and reservoirs initially at the same pressure. The upstream reservoir is then isolated from the sample and the downstream reservoir by the closing of a valve and pressurized to a higher pressure than the other two. The permeability measurement starts by re-opening the valve and monitoring the pressure decay in the upstream reservoir and the eventual pressure buildup in the downstream reservoir. As explained later in this paper, the sample permeability can be inferred from the rate at which the two reservoir pressures approach the final, equilibrium pressure in the system. When testing casing and annulus cement sections, as is done here, the measured permeability reflects the dominating contributions to effective wellbore permeability, typically flaws such as micro-annuli or fractures in the cement.

The pressure-pulse-decay method was first used by Brace et al. to measure the permeability of granite cores under high pressure [17]. The theory for test interpretation was further developed by Hsieh et al. [18], Dicker and Smits [19], and Jones [20] who solved the linear pressure diffusion equation by way of Laplace transforms, and Haskett et al. who generalized the solution to linear gas flow through integral transforms [21]. Nonlinear diffusion effects due to pressure-dependent material properties was explored by Marshall [22] while Hannon [23] developed extended models for analyzing heterogeneous cores and crushed samples. Pressure-pulse-decay models for measurements on fractured, dual porosity cores were recently discussed by Han et al. [24].

The main goal of this study is to further contribute to the knowledge of effective wellbore permeabilities by studying full-scale cemented annulus test sections, one of which has been retrieved from an offshore production well. Furthermore, it will be shown how transient measurements can be used as an alternative method for permeability and micro-annulus characterization in full-scale assemblies. An important motivation for the transient pressure-pulse-decay measurement is that it enables significantly quicker permeability characterization compared to the steady-state test

protocol. Especially in low-permeable test sections, it may be particularly difficult to establish truly steady-state conditions.

The outline of the paper is as follows. The two test sections are presented in more detail in the next section. Next, the necessary theory for interpreting the pressure-pulse-decay measurements is introduced, focusing on both uniform permeability and a discontinuous permeability model that better represents the pressure propagation through the two test sections studied in this paper. The discontinuous permeability model is calibrated to transient measurements in both test sections, before comparing effective permeabilities to those measured in steady-state seepage experiments. Finally, I provide a summary and the main conclusions of the paper.

2 Test Assemblies

Two full-scale cemented annulus test sections are studied in this paper. These are denoted "PWC Jig and Transition Joint", respectively, and are presented in more detail below.

2.1 PWC Jig. The first assembly to be studied consists of a 9 5/8-in. casing centralized inside a 13 5/8-in. casing. The distance between the inlet and outlet ports at either end of the assembly is 11.1 m, and one additional test port is positioned mid-way along the section. The assembly was constructed primarily for research purposes such as testing of cement verification methods and was cemented vertically in Nov. 2015. The PWC Jig is shown laying horizontally behind the test rack in Fig. 1.

2.2 Transition Joint. The second assembly studied herein is denoted transition joint and consists of a 9.4 m long section of a 9 5/8-in. casing inside a 13 3/8-in. casing. The transition joint is one of a number of casing-in-casing sections that were cut and retrieved from a production well in the Norwegian sector of the North Sea in 2018 as part of establishing the required surface plug in the well. A wellbore schematic showing the location of the transition joint is provided in Fig. 2.

Two of the retrieved sections are shown in Fig. 3, with the transition joint positioned to the right. The well was originally cemented in 1985 and had seen more than 30 years of production when it was abandoned in 2018. The transition joint contains the 9 5/8-in. and 13 3/8-in. annulus top-of-cement about mid-way along the length of the section. Previous analyses of the test section include surface re-logging [15,16] which indicated the transition from cement to mud from 4.5 m to 5.8 m measured from the bottom of the section. This part of the well was cemented by reverse circulating cement slurry down the annulus as the second stage of the primary cementing operation of the 9 5/8-in. casing. Furthermore, while the PWC Jig introduced above has been constructed for research purposes and never been in a live well, the transition

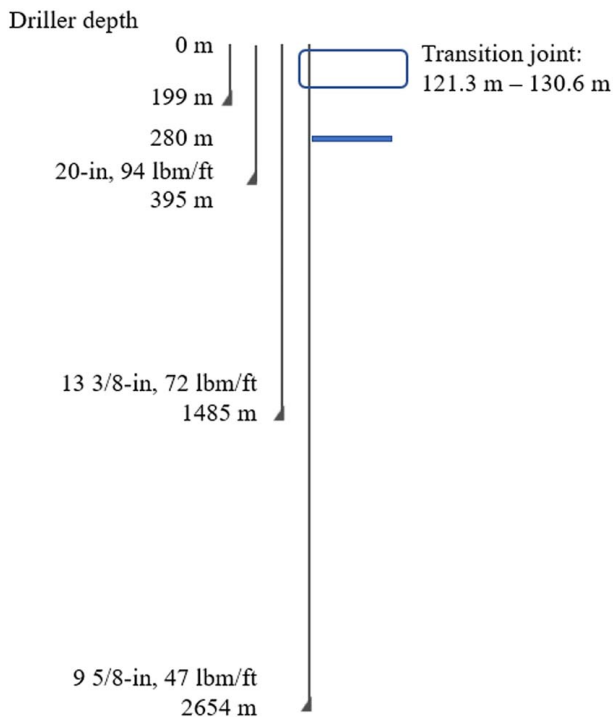**Fig. 1 The PWC Jig placed horizontally for pressure testing**

Fig. 4 Exposed top (left) and bottom (right) of the transition joint

joint has experienced drilling and production-related loads such as thermal shocks.

The exposed annulus cross sections at the top and bottom of the test section are shown in Fig. 4. The inner 9 5/8-in. casing is fully eccentered inside the 13 3/8-in. casing, with only the 9 5/8-in. casing collar providing an offset between the two casing walls away from the collar. The eccentricity is estimated to be approximately 0.63 based on the nominal dimensions of the 9 5/8-in. casing collar. The top of the test section contains a solid mass of settled weighting material above the top-of-cement. The bottom cross section to the right shows full cement coverage around the annulus and also significant contamination in the form of local heterogeneities. Previous observations of gas migration through the bottom cemented cross section indicated communication along both cement-casing interfaces, that is both along the outer wall of the inner casing and along the inner wall of the outer casing [16]. The ends of the sections have since been dressed with bulkheads to allow testing under pressure and to avoid further drying of the cement. A more detailed description of the transition joint, including an initial examination of the cement, can be found in Ref. [16].

Inlet and outlet ports have been mounted on the end caps of the assembly, ensuring full exposure of the entire annulus cross sections. In addition, a total of 14 pressure ports have been mounted along the length of the transition joint, spaced approximately every 1.2 m, with 7 ports accessing the wide side of the eccentric annulus and 7 ports accessing the narrow side.

3 Measurement Protocol

A combination of steady-state seepage measurements and transient pressure-pulse-decay measurements was performed on the two test sections described above. The measurements were all performed with the two assemblies in horizontal position, with pressure transmitters mounted at each available test port. The pressure transmitters have a working range of 0–60 bar and an accuracy of ±0.25% of the working range. Pressure was logged at a rate of mainly 1–5 Hz in the pressure-pulse-decay experiments. A temperature transmitter was also connected to the assemblies to monitor possible temperature developments over the course of the test program.

Steady-state seepage measurements were performed by connecting the inlet port to a test pump while maintaining the outlet port open. Once the measured pressure in the assembly was steady and a constant flowrate observed through the outlet port, the seepage rate was measured by collecting the effluent over a predefined time interval. The measurement series continued by repeating these measurements at different values of inlet pressure and possibly by varying the port used as the outlet port. These steady-state seepage measurements rely on achieving a steady flowrate through the test section which can be difficult to achieve in low-permeable test cells. Once the sections were fully saturated, the sections considered here required typically 20–30 min for stable flow at each pressure differential.

Fig. 2 Well schematic of the production well from where the transition joint was retrieved. The transition joint is a casing-in-casing section consisting of 9 5/8-in. production casing, annular cement, and 13 3/8-in. intermediate casing.

Fig. 3 Two cut and pulled sections from a North Sea well. The transition joint is shown to the right.

Transient pressure-pulse-decay measurements were performed by connecting an upstream fluid reservoir to the inlet port and a downstream fluid reservoir to the outlet port of the section to be tested. Liquid bottles, each of 114 l capacity, were used as upstream and downstream reservoirs. Pressure transmitters were mounted at the lines connecting the reservoirs to the test section and at pressure ports along the length of the test section. A set of valves were used to connect or isolate the fluid reservoirs and the test section.

In preparation for testing on each section, the compressive storage of the two reservoirs and of the test section was measured. The compressive storage of a closed vessel is taken as the ratio of an injected volume of fluid to the corresponding increase in vessel pressure and was measured by pressurizing the closed test section with water as the working fluid, followed by bleeding down the pressure in steps while measuring the effluent at each step. The compressive storages of the components are needed in order to fit the pressure decay model to the pressure measurements, as shown in the following section. A needle valve was used to take the pressure down in steps. The same procedure was performed to also measure the compressive storage of the two reservoirs.

Before starting a measurement, the two reservoirs and the test section were brought to the same initial pressure which varied between 5 bar and 45 bar in the tests performed in this study. Once stabilized, the valve between the upstream reservoir and the test section was closed and a test pump was used to increase the upstream reservoir pressure to a predefined, higher pressure than the test cell and the other reservoir. The test commenced by rapidly opening the valve and monitoring the propagation of the pressure pulse through the test section and the downstream reservoir. Once the pressure had stabilized throughout the system, the test was repeated at the same or a different initial pressure. If testing at the same initial pressure, the final, stabilized pressure at the end of the previous test was bled down before pressurizing to the initial pressure level. To identify differences in the permeability or the micro-annuli between the top and the bottom of the sections, pressure-pulse-decay experiments were performed in both directions, from bottom to top, and then from top to bottom of the sections. All measurements reported in this paper used water as working fluid.

Since the PWC Jig and the transition joint were both cemented vertically, I will refer to the *bottom* and *top* of the sections as seen when they were cemented. For the transition joint, in particular, this means that the material above the top-of-cement is located toward the top of this section. To measure the permeability of the sections, steady-state flow tests and transient pressure tests have been performed both from the bottom to the top and from the top to the bottom. Testing from bottom to top will be referred to as the standard test direction, and tests performed from top to bottom as tests performed in the reverse direction. As such, the standard test direction is considered most relevant for fluid migration in a well, that is toward the surface. An important motivation for also testing the sections in the reverse direction was to detect possible variations in permeability or equivalent micro-annulus size along the length of the sections. Finally, for the transition joint, tests have been performed with an applied pressure inside the inner casing. A constant pressure of 10, 20, or 30 bar has been applied to the casing to study how elastic expansion of the inner casing affected the measured permeability of the annulus cement both when performing steady-state measurements and transient pressure-pulse-decay experiments.

4 Model of Pressure-Pulse-Decay Experiments

The model for interpreting pressure-pulse-decay measurements, covering the cases of uniform, effective permeability and a discontinuous permeability profile, will be presented in this section. Both effective permeability and effective micro-annulus will be used to characterize the zonal isolation qualities of the annulus cement. The concept of micro-annulus is motivated by previous studies

that have found the cement-casing and cement-formation interfaces as likely leakage pathways, and that these pathways exhibit fracture-like responses to changes in stress and effective pressure [9]. While most of the literature on pressure-pulse-decay measurements use permeability, studies of cement-casing and cement-formation geometries use the concept of micro-annulus to characterize interface leakage pathways. The two concepts can be used interchangeably, as the effective permeability $\hat{k}$ and the equivalent effective micro-annulus $\hat{h}$ are related by

$$\hat{k}\hat{A} \rightarrow \frac{\hat{W}\hat{h}^3}{12} \tag{1}$$

where $\hat{A}$ is the cross-sectional area of the annulus and $\hat{W}$ is the circumference of the micro-annulus. Assuming the effective micro-annulus is located at the outer cement interface, $\hat{W} = 2\pi\hat{R}_o$ with $\hat{R}_o$ the inner radius of the outer casing.

4.1 Uniform Permeability. Consider first a test section of uniform permeability (or equivalent uniform micro-annulus size, as explained above) and assume that fluid flow through the section can be described by the Darcy flow equation:

$$\hat{v} = \frac{\hat{k}}{\hat{\mu}}\left(-\frac{d\hat{p}}{d\hat{x}}\right) \tag{2}$$

where $\hat{v}$ is the fluid velocity, $\hat{k}$ is the effective permeability, $\hat{\mu}$ is the fluid viscosity, and $d\hat{p}/d\hat{x}$ is the pressure gradient. Here, and in the following, a hat symbol is used to denote quantities with physical dimensions and units. Using the Darcy equation in combination with the principle of mass conservation, the pressure diffusion equation

$$\frac{d\hat{p}}{d\hat{t}} = \frac{\hat{k}}{\hat{\mu}\hat{c}}\frac{d^2\hat{p}}{d\hat{x}^2} \tag{3}$$

is obtained for the pressure evolution inside the test cell with compressibility $\hat{c}$. It is here assumed that the material and fluid properties $\hat{k}$, $\hat{\mu}$, and $\hat{c}$ can be considered constant within the test pressures of each experiment; in this idealized case, the experiments are described by a linear diffusion equation.

The test cell is connected to an upstream and a downstream reservoir of known initial volumes. The upstream reservoir volume will be denoted by $\hat{V}_u$ and the effective compressibility of the upstream reservoir and water by $\hat{c}_{res,u}$. The same quantities $\hat{V}_d$ and $\hat{c}_{res,d}$ are defined for the downstream reservoir. Boundary conditions for the pressure diffusion equation (3) are derived by considering the flow of fluid from the upstream reservoir to the test cell and the associated decrease in upstream reservoir pressure, $\hat{p}_u$:

$$\hat{V}_u\hat{c}_{res,u}\frac{d\hat{p}_u}{d\hat{t}} = \frac{\hat{k}\hat{A}}{\hat{\mu}}\frac{d\hat{p}}{d\hat{x}} \tag{4}$$

where again the Darcy equation has been substituted for the bulk velocity. At the downstream reservoir, the corresponding boundary condition reads

$$\hat{V}_d\hat{c}_{res,d}\frac{d\hat{p}_d}{d\hat{t}} = -\frac{\hat{k}\hat{A}}{\hat{\mu}}\frac{d\hat{p}}{d\hat{x}} \tag{5}$$

As initial conditions, it is assumed that the test cell and the downstream reservoir are maintained at stable and uniform pressure $\hat{p}_d(\hat{t}=0)$. The upstream reservoir is isolated from the rest of the assembly by a closed valve and pressurized to an elevated pressure $\hat{p}_u(\hat{t}=0) > \hat{p}_d(\hat{t}=0)$. The valve is opened and the test starts at $\hat{t}=0$.

4.2 Dimensionless Equations and Analytical Solution. To proceed, the governing equations are expressed in terms of the dimensionless pressure, time, and position defined as follows:

$$p = \frac{\hat{p} - \hat{p}_d(0)}{\hat{p}_u(0) - \hat{p}_d(0)}$$

$$t = \frac{\hat{k}}{\hat{\mu}\hat{c}\hat{L}^2}\hat{t}$$

$$x = \hat{x}/\hat{L}$$

where $\hat{L}$ is taken to be the axial length of the test cell. Expressed in terms of the dimensionless quantities, the governing equation and boundary conditions are:

$$\frac{dp}{dt} = \frac{d^2p}{dx^2} \qquad (6a)$$

$$\gamma_u \frac{dp}{dx} = \frac{dp_u}{dt} \quad \text{at } x = 0 \qquad (6b)$$

$$\gamma_d \frac{dp}{dx} = -\frac{dp_d}{dt} \text{ at } x = 1 \qquad (6c)$$

Here, $\gamma_u = \hat{c}\hat{V}/(\hat{c}_{\text{res},u}\hat{V}_u)$ denotes the ratio of the compressive storage in the test cell to that of the upstream reservoir. The test cell volume is denoted by $\hat{V}$. Similarly, γ_d denotes the compressive storage ratio of the test cell to the downstream reservoir. The initial condition for the dimensionless pressure is now $p(x=0, t=0)=1$ and $p(x>0, t=0)=0$.

The solution of the diffusion equation above is most readily obtained by Laplace transform [25]. Combining the general solution of the pressure diffusion equation with the boundary conditions of Eqs. (6b) and (6c), Hsieh et al. [18] and Dicker and Smits [19] found the following result for the pressure difference between the two reservoirs:

$$p_u(t) - p_d(t)$$
$$= 2\sum_{m=1}^{\infty} \frac{\left[\gamma_u(\gamma_d^2 + \theta_m^2) - (-1)^m \gamma_d \sqrt{(\gamma_u^2 + \theta_m^2)(\gamma_d^2 + \theta_m^2)}\right]\exp(-\theta_m^2 t)}{\theta_m^4 + \theta_m^2(\gamma_u + \gamma_u^2 + \gamma_d + \gamma_d^2) + \gamma_u\gamma_d(\gamma_u + \gamma_d + \gamma_u\gamma_d)}$$
$$(7)$$

where θ_m are the roots of the equation

$$\tan\theta = \frac{(\gamma_u + \gamma_d)\theta}{\theta^2 - \gamma_u\gamma_d} \qquad (8)$$

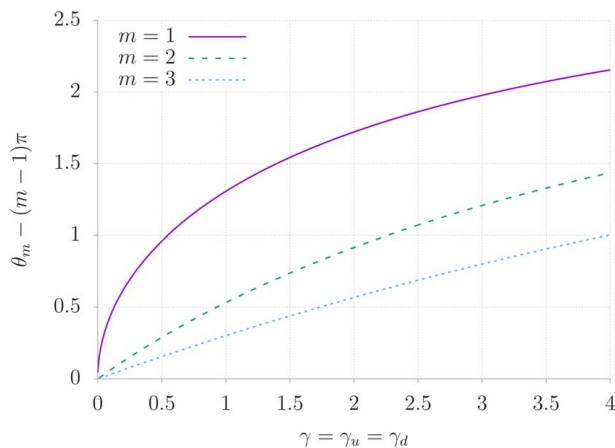In this work, the roots of Eq. (8) are found using the bisection method of Ref. [26]. This method works by repeatedly bisecting an interval known to contain the root of the equation. Focusing now on configurations where the two reservoirs are identical, we plot the first three roots $\theta_m - (m-1)\pi$, as function of $\gamma = \gamma_u = \gamma_d$ in Fig. 5.

At "late-times" in the pressure-pulse-decay experiment, the pressure difference between the reservoirs is dominated by the first term in the sum in Eq. (7), resulting in single exponential behavior. This is illustrated in Fig. 6, where the full solution is seen to follow a single exponential solution represented by the dotted line following an initial transient. It is observed that the duration of the initial transient increases with increasing compressive storage of the test cell relative to the reservoirs. However, at later times ($t \geq 0.1$ for the cases considered here), the pressure difference can be approximated by

$$\ln\big(p_u(t) - p_d(t)\big) = \text{constant} - \theta_1^2 t \qquad (9)$$

where θ_1 is the first, non-zero root of Eq. (8).

4.3 Heterogeneous Permeability Model.
As full-scale test sections may exhibit locally varying permeability, the model introduced above will now be generalized to allow for a discontinuous permeability inside the sample, represented by a step change from a constant permeability to a different constant permeability at a position ℓ, measured from the bottom of the test cell. Following the model derived by Hannon [23], denote the permeability in $0 < x < \ell$ by $\hat{k}_1$ and that of the adjacent section $\ell < x < 1$ by $\hat{k}_2$. The ratio of the permeabilities is denoted $\lambda^2 = \hat{k}_1/\hat{k}_2$. At $x = \ell$, continuity of pressure and of flux is required, resulting in two additional boundary conditions at the interface:

$$\lim_{x \to \ell^-} p(x, t) = \lim_{x \to \ell^+} p(x, t)$$

$$\lambda^2 \frac{\partial p}{\partial x}\bigg|_{x \to \ell^-} = \frac{\partial p}{\partial x}\bigg|_{x \to \ell^+}$$

As per Ref. [23], the dimensionless time is defined using $\hat{k}_1$ as scale for the permeability. Consequently, the pressure diffusion equation in $0 < x < \ell$ and the boundary condition at $x = 0$ are the same as before, Eqs. (6a) and (6b). These equations are combined with the following diffusion equation in $\ell < x < 1$ and boundary condition at $x = 1$:

$$\frac{\partial p}{\partial t} = \frac{1}{\lambda^2}\frac{\partial^2 p}{\partial x^2}$$

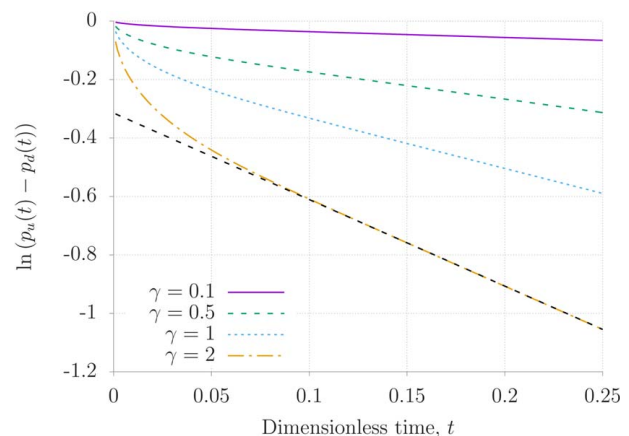$$\frac{\partial p_d}{\partial t} = -\frac{\gamma_d}{\lambda^2}\frac{\partial p}{\partial x}$$

Fig. 5 The first three roots of Eq. (8) as function of compressive storage ratio γ. The ratio is assumed equal for the upstream and downstream reservoirs, $\gamma_u = \gamma_d$.

Fig. 6 Numerical evaluation of the reservoir pressure difference for different values of γ for the uniform permeability case. The upstream and downstream reservoirs are here assumed to have the same compressive storage ratio. The black dotted line is obtained from Eq. (9), with θ_1 the first root of Eq. (8) for $\gamma = 2$.

The linear pressure diffusion equation is solved with a Laplace transform method, and numerical inversion by the Stehfest algorithm is used to obtain the test cell and reservoir pressures in the time domain [27].

In Fig. 7, the effects of permeability heterogeneity on the pressure evolution (solid lines) is demonstrated by comparing with uniform permeability results (dashed lines). To facilitate the comparison, it is assumed that $\hat{k}_1$ is equal to the permeability of the uniform sample, so the time scale is the same for the two simulations. Finally, $\gamma_u = \gamma_d = 2$ in this example, and the heterogeneous sample is assumed to have a permeability discontinuity at $\ell = 0.5$, with permeability ratio $\lambda = 0.25$. In addition to the upstream and downstream reservoirs, the pressure evaluated at $x = \ell$ is also plotted for the two models. As expected, the early-time evolution of the upstream pressure is the same in the two models, since the permeability of the interval $0 < x < \ell$ is the same. The evolution toward the final test pressure of $p_f = \gamma_d/(\gamma_u + \gamma_d + \gamma_u \gamma_d) = 1/4$ is more rapid for the heterogeneous sample, since the permeability in $\ell < x < 1$ is 16 times higher than that of the uniform model. As a result, the mid-point pressure in the heterogeneous model follows more closely that of the downstream reservoir, due to the high permeability and better connectivity.

In Fig. 8, the same system as in Fig. 7 is considered, but now with a reversed pressure pulse direction. Thus, the pulse propagates from the "downstream reservoir" through the high-permeability segment in $\ell < x < 1$ and to the "upstream reservoir" through the low-permeability segment in $0 < x < \ell$. As expected, a reversed trend

can be observed, where now the downstream and mid-point pressures approach the same value very quickly, followed by a slower decay toward the final pressure. The apparent sensitivity to test direction seen in Figs. 7 and 8 can be used to identify permeability variations along test sections, as will be shown when discussing test results below.

This heterogeneous permeability model is fitted to pressure measurements by determining the position of the permeability discontinuity, ℓ, the permeability ratio, λ^2, and also the magnitude of $\hat{k}_1$. To connect $\hat{k}_1$ to the effective permeability, $\hat{k}_{eff}$, that is derived from the pressure difference across the entire test specimen, I take $\hat{k}_1 = \hat{k}_{eff}[\lambda^2 + \ell(1 - \lambda^2)]$. Here, it is assumed that the flux corresponding to $\hat{k}_{eff}$ and a unit pressure drop over the entire specimen are the same as the flux corresponding to piece-wise constant pressure drops in the sections of $\hat{k}_1$ and $\hat{k}_2$. This assumption connects $\hat{k}_1$ to the pressure drop between the reservoirs. Finally, λ and ℓ are determined iteratively by fitting model predictions to the pressure measurements.

5 PWC Jig Measurements

5.1 Steady-State Seepage Measurements. To determine the effective micro-annulus size from steady-state measurements, a constant pressure difference $\Delta \hat{p}$ was maintained across the test cell, and the resulting steady-state flow rate $\hat{Q}$ was measured at the outlet port. The measurements were used to determine the micro-annulus size $\hat{h}$ using the cubic law equation

$$\hat{Q} = \frac{\hat{W}\hat{h}^3}{12\hat{\mu}} \frac{\Delta \hat{p}}{\hat{L}} \tag{10}$$

Here, $\hat{W}$ is the circumference of the micro-annulus assumed to be at the cement-outer casing interface and as defined in Eq. (1). The distance between the inlet and outlet ports is denoted $\hat{L}$. A summary of the test results when testing in the standard direction (from bottom to top) is provided in Table 1.

If the permeability or micro-annulus was uniform between inlet and outlet ports, we would expect the mid-point pressure to be the average of the inlet and outlet pressures. However, it is observed in Table 1 that the mid-point pressure was systematically lower than the average, suggesting higher permeability and larger micro-annulus size in the upper part of the section, between the mid-point and the outlet ports in Table 1. A tendency for increasing micro-annulus size with increasing test pressures is also seen, attributed mainly to elastic expansion of the casing. In Table 2, steady-state seepage measurements are listed for the reverse flow direction. The "outlet" pressure specified in the table was measured by a pressure transmitter in close proximity to the open outlet port. A considerable pressure was recorded by the transmitter, indicating significant choking through the outlet port. No such choking was observed for the tests reported in Table 1 and the outlet pressure therefore set to zero when testing in that direction. For the effective micro-annulus size listed in Table 2, the cubic law in Eq. (10) is used together with the inlet and outlet pressures in Table 2. The same effective micro-annulus sizes were found when reversing the flow (Table 1). Consistent with the results above is the
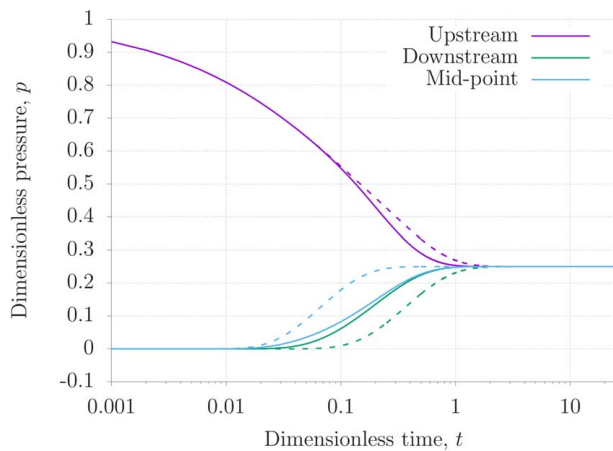
Fig. 7 Comparison of model pressure evolution for a uniform test cell (dotted lines) to that of a heterogeneous cell (solid lines) characterized by $\lambda = 0.25$ and $\ell = 0.5$. Here, $\gamma_u = \gamma_d = 2$.
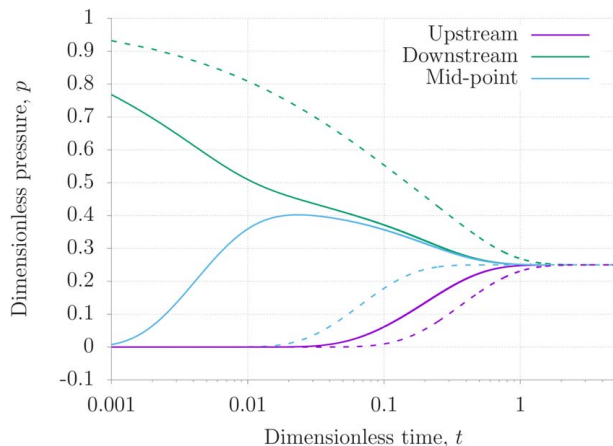
Fig. 8 The same configuration as in Fig. 7, but with reversed pressure pulse direction

Table 1 Micro-annulus size from steady-state leakage tests in the PWC Jig obtained using Eq. (10) when testing from bottom to top

Pressure (bar)			Flowrate	Micro-annulus
Inlet	Mid-point	Outlet	(ml/min)	(μm)
16.96	3.59	0	165	60
23.96	5.63	0	262	63
32.96	8.63	0	406	65
42.81	12.65	0	615	69

Table 2 Micro-annulus size from steady-state leakage tests in the PWC Jig obtained using Eq. (10) when testing from top to bottom

Pressure (bar)			Flowrate (ml/min)	Micro-annulus (μm)
Inlet	Mid-point	Outlet		
16.53	14.19	2.44	156	63
22.68	19.73	3.83	230	65
33.63	29.42	7.85	376	69
45.78	41.10	11.86	597	73

observation that the top part of the section (between inlet and mid-point in Table 2) resulted in a smaller pressure drop than the bottom part. This suggests less flow restriction between the inlet and mid-point in Table 2 compared to between mid-point and the outlet. In the following section, the permeability differences between the upper and lower parts of the test section will be studied in more detail using the transient pressure records.

5.2 Pressure-Pulse-Decay Measurements. Measurements used to determine the compressive storage of the upstream and downstream reservoirs and of the PWC Jig are shown in Fig. 9. As indicated in the equation in the figure, the inverse of the slope is taken as the compressive storage. For PWC Jig, $\hat{c}\hat{V} = 1.71 \times 10^{-10}$ m³/Pa, while the reservoirs are taken as $\hat{c}_{res,u}\hat{V}_u = \hat{c}_{res,d}\hat{V}_d = 7.90 \times 10^{-11}$ m³/Pa. Consequently, the ratio of compressive storage between the test cell and the reservoirs is approximately 2.16. The first root of Eq. (8) for this value of γ is $\theta_1 = 1.769$, which is found using the bisection method.

In Fig. 10, the measured pressure difference across the test cell is plotted as function of time, $\hat{t}$, and for different initial pressures in the downstream reservoir and test cell. Initially, the upstream reservoir pressure was approximately 10 bar higher than the test cell and downstream reservoir in each test case. The black dashed lines that overlay the measurements indicate the curve fit to the linear portion ("late time") of the measurements. Using Eq. (9) and the definition of dimensionless time, the slope of the curve is given by

$$\text{slope} = -\frac{\theta_1^2 \hat{k}\hat{A}}{\hat{\mu}\hat{L}\hat{c}\hat{V}} \tag{11}$$

when plotted against time. The permeability $\hat{k}$ is then found from the slope, using Eq. (11). The permeabilities found from Fig. 10
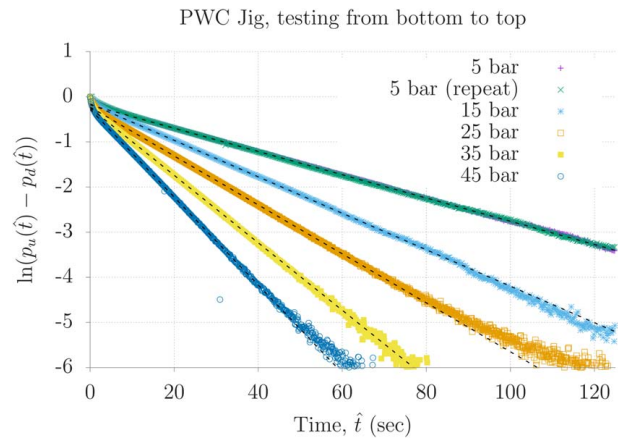
Fig. 10 Measured pressure differences between upstream and downstream reservoir as function of time for different initial pressures and testing in the standard direction with the upstream reservoir connected to the bottom end. The legend indicates initial downstream and test cell pressures. The upstream reservoir was initially pressurized to 10 bar above the test cell and the downstream reservoir.

and the equivalent micro-annulus widths are listed in Table 3. As seen from the slope of the curves in Fig. 10 and as reflected in the permeability and micro-annuli listed in Table 3, there was an increase in measured permeability and micro-annulus gap width with increasing test pressures. Furthermore, when comparing similar test pressures between Table 3 and the steady-state measurements in Table 1, one observes good quantitative agreement when comparing similar average pressure conditions inside the test cell.

To further explore the pressure-dependence indicated in Table 3, the micro-annulus size is plotted as function of initial test pressure in Fig. 11. A linear increase in effective micro-annulus size with increasing initial pressure is observed, and measurements are fitted to a linear function of the form $\hat{h}(\hat{p}) = \hat{h}_0 + \Delta\hat{h}\hat{p}$, where h_0 is the residual micro-annulus in the absence of applied annulus pressure. A least-squares curve fit results in $\hat{h}_0 = 54$ μm and $\Delta\hat{h} \approx 0.8$ μm/bar based on these measurements.

Similar trends of micro-annulus size have been reported by Stormont et al. previously. Their results show a decrease in gap size with increasing external confining pressure, and an increase in gap size with increasing pore pressure under constant confining pressure [9]. To model the effect of increasing test pressure on micro-annulus size seen in Fig. 11, one may assume that the dominant effect of pressure is to radially expand the outer casing. In this case, the pressure-dependent micro-annulus is $\hat{h}(\hat{p}) = \hat{h}_0 + \hat{u}_r(\hat{p})$, where the thin-walled closed-ends cylinder result $\hat{u}_r(\hat{p}) = (1 - \nu/2)\hat{p}\hat{R}^2/(\hat{E}\hat{\delta})$ may be used to estimate the radial expansion of the casing. Here, ν and $\hat{E}$ are Poisson's ratio and Young's modulus of the casing, respectively, $\hat{\delta}$ is the wall thickness, and $\hat{R}$ is the average radius of the outer casing. Using standard
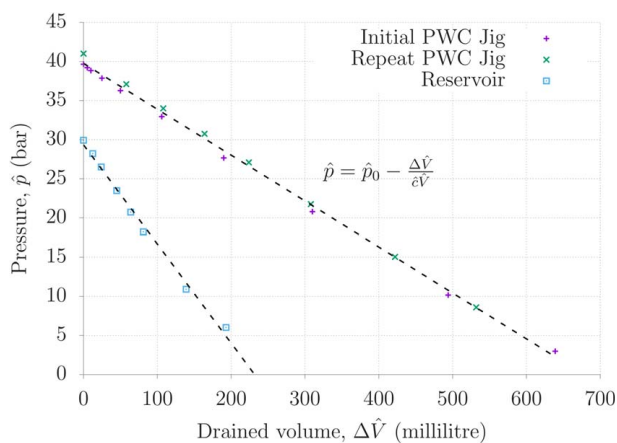

Fig. 9 Compressive storage of PWC Jig and the reservoirs. The equation in the plot gives the relationship between the pressure change from the initial value $\hat{p}_0$ and the corresponding drained volume $\Delta\hat{V}$ through the compressive storage $\hat{c}\hat{V}$.

Table 3 Permeability and micro-annulus widths measured from pressure decay test when testing in the standard direction (from bottom to top)

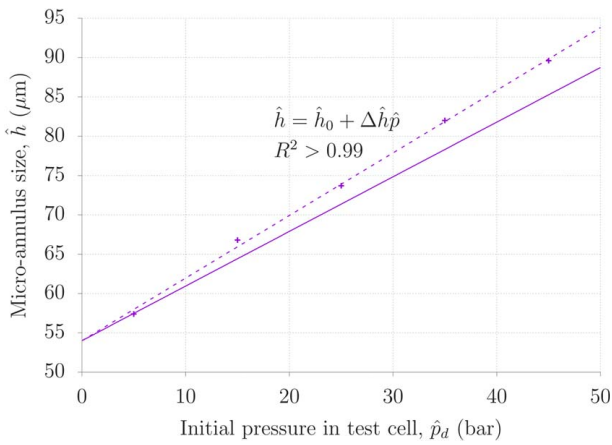| Initial pressures (bar)		Permeability, $\hat{k}$ (m²)	Micro-annulus, $\hat{h}$ (μm)
$\hat{p}_u$	$\hat{p}_d$		
15	5	5.10×10^{-13}	57.4
25	15	8.00×10^{-13}	66.8
35	25	1.07×10^{-12}	73.7
45	35	1.48×10^{-12}	82.0
55	45	1.93×10^{-12}	89.6

Fig. 11 Increase in effective micro-annulus gap with increasing initial test pressures. The dashed line is the best linear curve fit to the measurements and the solid line represents predicted micro-annulus based on radial expansion of outer casing.

values for a 13 5/8-in. casing, $\hat{u}_r(\hat{p})/\hat{p} \approx 0.7$ μm/bar, represented by the solid line in Fig. 11. Although not in complete numerical agreement with the pressure-dependence seen in the figure, the simplistic linear elastic model still captures the correct qualitative linear behavior and supports the hypothesis of dominant flow along discrete micro-annulus paths. The difference between the elastic model predictions and the measured values could be due to the existence of additional leakage paths not reflected in the simpler model, such as paths along the interface between the cement and the inner casing, or that new leakage paths are opened as the test pressure increases.

5.3 Permeability Variation. To investigate permeability variations between the bottom and top part of the jig, consider as a specific example the full time-based measurement series for the test with 25 bar upstream reservoir pressure and 15 bar downstream reservoir pressure, shown in Fig. 12. The points in the figure are pressure measurements and the dashed lines are results of the uniform permeability model, using the permeability from Table 3 as input. A comparison shows that the measured upstream pressure decreased more slowly than that predicted by the uniform permeability model. At the same time, the measured pressure at the mid-
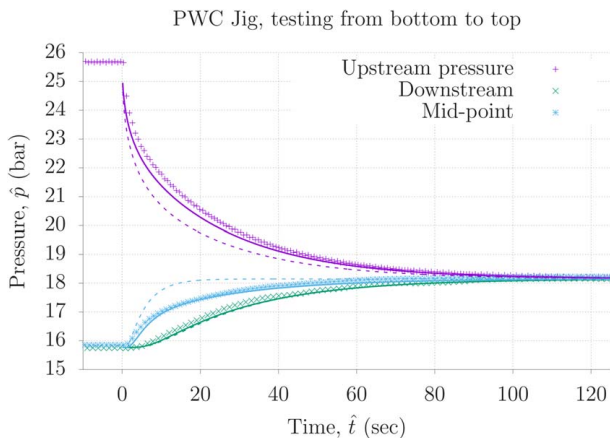

Fig. 12 Comparison of pressure measurements (points) with model predictions based on uniform permeability (dashed lines) and a heterogeneous permeability model (solid lines) for the _PWC Jig_. The initial pressure in the test jig and the downstream reservoir was close to 15 bar, while the upstream reservoir was pressurized to approximately 25 bar.
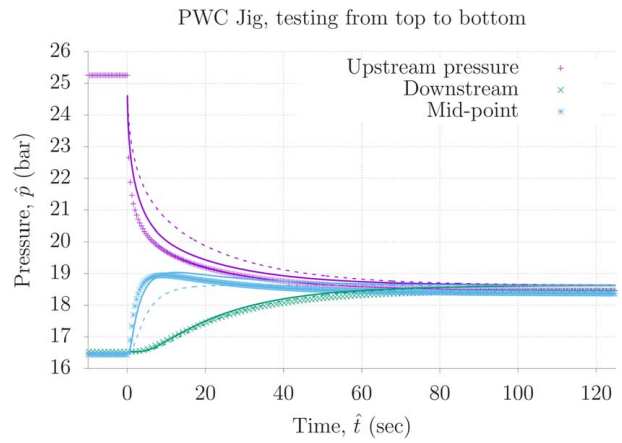

Fig. 13 Comparison of pressure measurements (points) with model predictions based on uniform permeability (dashed lines) and a heterogeneous permeability model (solid lines) for the _PWC Jig_ in the reverse test direction (from top to bottom). The initial pressure in the test jig and the downstream reservoir was close to 15 bar, while the upstream reservoir was pressurized to approximately 25 bar.

point approached the final pressure slower than the model predictions. The downstream pressure measurements however agree well with the response predicted by the uniform permeability model. The solid lines in Fig. 12 correspond to the results of the heterogeneous permeability model where now $\lambda = 0.55$ and $\ell = 0.4$ in that model. This value of ℓ suggests that the permeability transition occurs at a distance $0.4\hat{L}$ from the bottom of the section, with $\hat{L}$ the total section length. The permeability of the bottom section is taken as $\hat{k}_1 = \hat{k}_{\mathrm{eff}}[\lambda^2 + \ell(1 - \lambda^2)]$, where $\hat{k}_{\mathrm{eff}} = 8.0 \times 10^{-13}$ m² is the effective permeability from Table 3 for the 25 bar and 15 bar initial reservoir pressure. This parameter combination produces the solid lines in Fig. 12, suggesting that $\hat{k}_1 \approx 0.58\hat{k}_{\mathrm{eff}}$ and $\hat{k}_2 \approx 1.92\hat{k}_{\mathrm{eff}}$, i.e., a ratio of approximately 3.3 between the high-permeable upper part and the low-permeable bottom part of the PWC Jig. In terms of micro-annulus size, this parametrization corresponds to approximately $56\,\mu$m gap size in the bottom part of the jig and $83\,\mu$m in the top part. When comparing the solid lines (heterogeneous permeability model) and the dashed lines (uniform permeability model) to the measurements (points) in Fig. 12, it is seen that heterogeneous model better reflects the pressure decay than the uniform model does.

To confirm the characterization of the test section permeability, the time-based measurement series for the reverse test direction is shown in Fig. 13. The trends seen in Fig. 13 from comparing measurements to the uniform and the heterogeneous models confirm the observation of higher permeability in the upper part of the section. The heterogeneous permeability model, using the same parametrization as above, i.e., $\lambda = 0.55$ and $\ell = 0.4$, results in an improved quantitative fit, as seen from the solid lines in Fig. 13.

6 Transition Joint Measurements

As per the PWC Jig, also the transition joint was tested from bottom to top and in the reverse direction from top to bottom in order to identify and confirm spatial variations in the permeability. From previous surface re-logging of the section [15,16], the transition between annulus cement and the material above the cement has been found to occur between approximately 4.5 m and 5.8 m measured from the bottom of the test section. Previous pressure measurements have indicated that the material above the cement does not provide any significant resistance to flow, whereas the cement in the bottom half covers the entire eccentric cross section and provides a better seal. These observations motivate a representation of

Table 4 Measured permeability and micro-annulus from steady-state leakage tests, using the difference between inlet and outlet pressures for approximating the friction pressure gradient

Pressure (bar)			Flowrate (ml/min)	Micro-annulus (μm)
Inlet	Outlet	Casing		
34.70	0	0	51.6	31
34.98	0	0	44.0	29
34.64	0	10.12	36.9	27
34.39	0	20.60	30.7	26
33.09	0	30.45	24.7	24

the test section as a sample with discontinuous permeability in the region of the top-of-cement. For the transition joint, steady state and transient pressure measurements have also been performed both with no internal casing pressure and with approximately 10, 20, and 30 bar internal casing pressure.

6.1 Steady-State Seepage Measurements. In Table 4, stable flowrate measurements are reported for varying internal casing pressure at nearly constant inlet pressure applied to the bottom of the section. As expected, the measurements show a decline in leakage rate as the inner casing pressure increases. This observation can be attributed to elastic expansion of the inner casing in response to the pressure, and a subsequent compression of the annular cement and reduction in micro-annulus size.

6.2 Pressure-Pulse-Decay Measurements. To facilitate the pressure-pulse-decay analysis of the transition joint, the compressive storage of the test section and the liquid reservoirs were determined following the same procedure as for the PWC Jig. The results for the test section and the bottles are shown in Fig. 14. As before, the compressive storage is extracted from the slope of the dotted lines which are linear curve fits to the measurements. I find $\hat{c}\hat{V} = 2.1 \times 10^{-10}$ m^3/Pa for the test cell and $\hat{c}_{res,u}\hat{V}_u = \hat{c}_{res,d}\hat{V}_d = 7.46 \times 10^{-11}$ m^3/Pa for the reservoirs. The storage ratio is found to be higher than for the PWC Jig, $\gamma = 2.81$. The corresponding first root of Eq. (8) is found to be $\theta_1 = 1.936$ using the bisection method.

Pressure-pulse-decay test results with no internal casing pressure (0 bar) and with applied, constant internal casing pressure (30 bar) are shown in Fig. 15. The standard test direction (from bottom to top) was used, with the upstream reservoir connected to the bottom of the section. Comparing first the results with no applied pressure inside the casing, the same trend as per the PWC Jig test
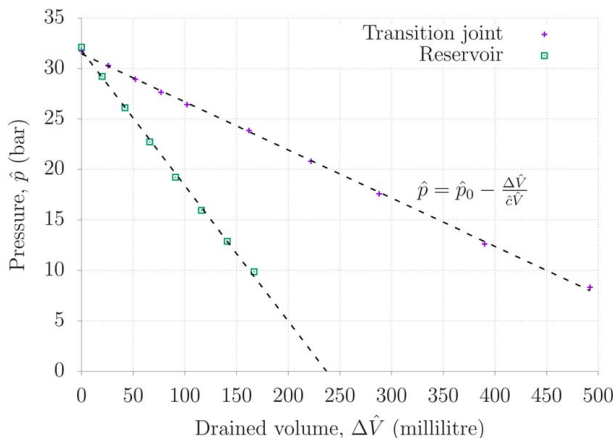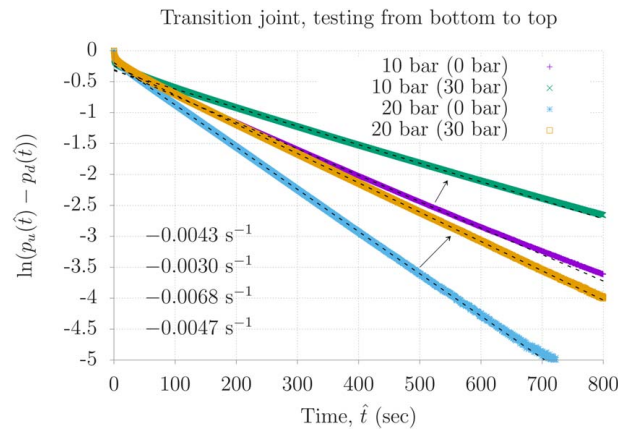

Fig. 15 Measured pressure differences between upstream and downstream reservoir as function of time for different combinations of initial upstream and downstream pressures. The standard test direction (from bottom to top) was used, with the upstream reservoir connected to the bottom end of the test section. The legend indicates initial downstream and test cell pressures with inner casing pressure specified in the parentheses. The upstream reservoir was initially pressurized to 10 bar above the test cell and the downstream reservoir. The numbers on the lower left corner correspond to slopes of the dashed lines, listed for the measurements in the same order as per the entries in the legend.

section is observed, namely, a steeper slope at the higher test pressure. This suggests a higher effective permeability at 20 bar compared to 10 bar initial pressure. Also included in the lower left of the figure are the slopes of the dashed lines. The values are listed for the measurements in the same order, from top to bottom, as per the entries in the legend. Fitting to the "late-time" measurements generally produced R^2 values equal to or larger than 0.99.

Application of inner casing (borehole) pressure can affect the cement log response in the field, potentially improving the acoustic contact between casing and annulus material. To test whether an internal casing pressure will affect the effective permeability of the transition joint, pressure-pulse-decay and steady-state seepage measurements have been performed also with 30 bar internal casing pressure. While the surface re-logging did not identify a distinct change in acoustic properties of the annulus material when logged with inner casing pressure [15,16], the permeability is seen to decrease slightly with increasing borehole pressure, as indicated by the arrows in Fig. 15. Combining the calculated slopes from Fig. 15 with the compressive storage of the reservoirs and the test section, the effective permeabilities and equivalent micro-annulus widths in Table 5 are obtained. Once again, the annular cross-sectional area between the production casing and the outer intermediate casing is used as basis for determining the permeability values in Table 5, and the micro-annulus is assumed located at the interface between the annulus cement and the inner wall of the outer 13 3/8-in. casing. The effective permeabilities are about 2 orders of magnitude greater than the permeability measured from intact

Fig. 14 Compressive storage of transition joint and bottles used as upstream and downstream reservoirs

Table 5 Measured permeability and equivalent micro-annulus for the transition joint when testing from bottom to top

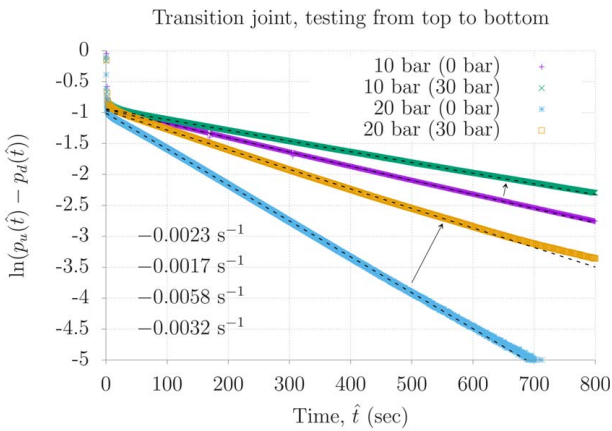| Initial pressures (bar)			Permeability, $\hat{k}$ (m^2)	Micro-annulus, $\hat{h}$ (μm)
$\hat{p}_u$	$\hat{p}_d$	$\hat{p}_{csg}$		
20	10	0	7.43×10^{-14}	30.2
20	10	30	5.21×10^{-14}	26.8
30	20	0	1.19×10^{-13}	35.2
30	20	30	8.24×10^{-14}	31.2

Fig. 16 Measured pressure differences between upstream and downstream reservoir as function of time for different combinations of initial upstream and downstream pressures. The reverse test direction (from top to bottom) was used. The legend indicates initial downstream and test cell pressures with inner casing pressure specified in the parentheses. The upstream reservoir was initially pressurized to 10 bar above the test cell and the downstream reservoir. The numbers on the lower left corner correspond to slopes of the dashed lines, listed for the measurements in the same order as per the entries in the legend.
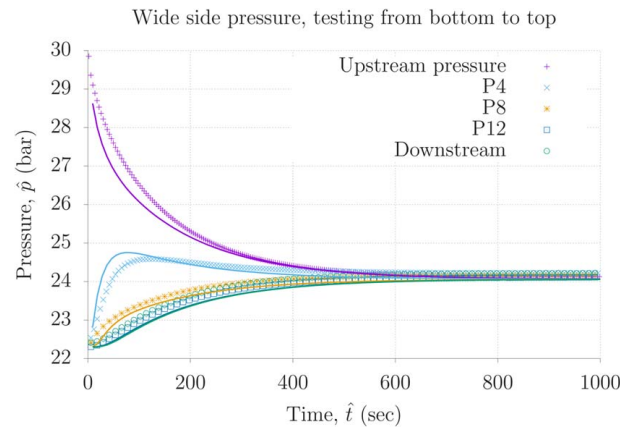

Fig. 17 Comparison of pressure measurements at the two reservoirs and at three locations along the wide side of the test cell annulus (points) with model predictions based on the heterogeneous permeability model (solid lines) for the transition joint. The initial pressure in the test jig and the downstream reservoir was close to 15 bar, while the upstream reservoir was pressurized to approximately 25 bar. The heterogeneous pressure diffusion model is parameterized by $\lambda = 0.2$ and $\ell = 0.575$.

cement cores from the bottom of the transition joint [28], supporting the observation that cement-casing interfaces and not bulk cement are likely the dominating annular flow paths, in agreement with previous works such as Ref. [6]. Furthermore, the effective micro-annulus sizes in Table 5 are within the range of that determined from effective wellbore permeabilities, as presented in Ref. [9].

Results from pressure-pulse-decay measurements when testing in the opposite direction are shown in Fig. 16. As per Fig. 15, here the slopes of the dashed lines are included in the lower left of the figure. The values are listed for the measurements in the same order, from top to bottom, as per the entries in the legend. The "late-time" measurements generally produced R^2 values equal to or larger than 0.99.

The results are qualitatively similar to those when testing the standard direction and one observes a steeper slope for the higher initial test pressure and a reduction in negative slope when pressure is applied inside the casing. A difference in the early-time behavior in Fig. 16 is noted when comparing to Fig. 15, suggesting a more rapid upstream pressure decrease when testing from top to bottom. Finally, effective permeabilities and equivalent micro-annuli widths based on Fig. 16 are listed in Table 6.

6.3 Permeability Variation. Finally, to study the variation in permeability between the bottom cemented half of the section and the permeability of the solid mass above the top-of-cement, consider the time-based pressure measurements acquired at intermediate test ports between the upstream and downstream reservoirs. As specified above, a total of 14 ports were drilled into the section, with even-numbered test ports drilled into the wide side of the eccentric

annulus and odd-numbered ports into the narrow side. The test ports were positioned approximately every 1.2 m along the section, with each port drilled across the annulus to access both casing-cement interfaces. In the following, I will show pressure measurements from the two reservoirs and three pairs of pressure ports along the test section. Here, pressure ports P3 and P4 are positioned 2.4 m from the bottom of the test section, accessing the narrow and wide sector of the annulus, respectively. Ports P7 and P8 are positioned 4.7 m from the bottom, while ports P11 and P12 are 7.1 m from the bottom. Previous results suggested that P7 and P8 are in the transition zone between cement and the solid mass above the top-of-cement, while P11 and P12 are above the top-of-cement.

In Figs. 17 and 18, pressure records are plotted for a test with approximately 22 bar initial pressure in the test cell and the downstream reservoir, and approximately 30 bar initial pressure in the upstream reservoir. The upstream reservoir was connected to the cemented bottom end of the transition joint. Minor differences between the opposite side P3 and P4 ports and the opposite side P7 and P8 ports are noted, suggesting slightly better communication between the upstream reservoir and the pressure ports on the narrow side compared to the wide side. The pressure at ports P7 and P8 and at ports P11 and P12 is also seen to follow the downstream reservoir

Table 6 Measured permeability and micro-annulus from pressure decay test when testing from top to bottom

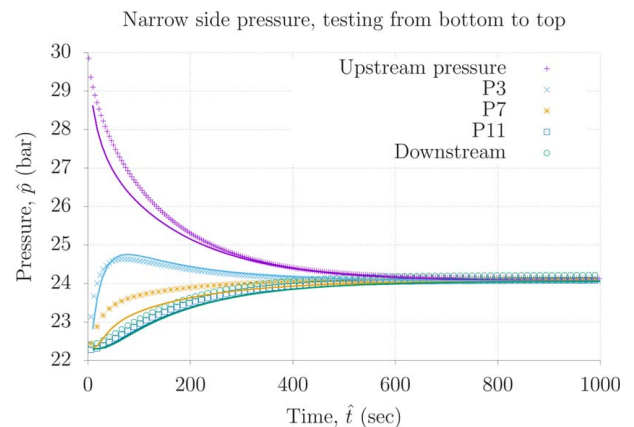| Initial pressures (bar)			Permeability, $\hat{k}$ (m²)	Micro-annulus, $\hat{h}$ (μm)
$\hat{p}_u$	$\hat{p}_d$	$\hat{p}_{csg}$		
20	10	0	3.99×10^{-14}	24.5
20	10	30	3.01×10^{-14}	22.3
30	20	0	1.01×10^{-13}	33.4
30	20	30	5.50×10^{-14}	27.3

Fig. 18 The configuration is the same as in Fig. 17, but the intermediate pressure measurements are now acquired from the narrow side of the test cell annulus
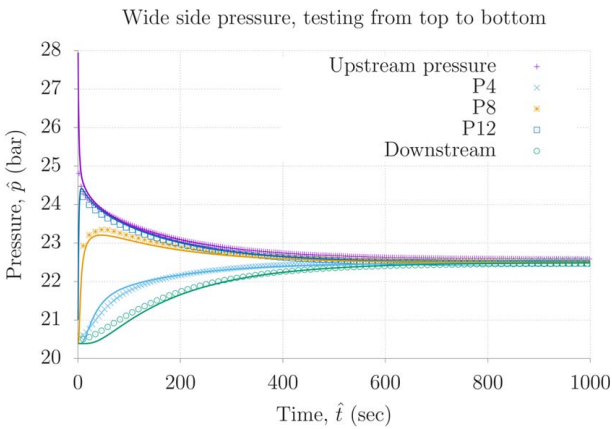
Fig. 19 The configuration is the same as in Fig. 17, but now in the reverse direction (the upstream reservoir connected to the top ("mud") part of the test section and the downstream reservoir to the bottom, cemented end)

pressure closely, confirming high permeability and nearly immediate pressure communication in the upper part of the test section, around and above the cemented interval.

Figures 19 and 20 correspond to testing in the reverse direction. Again, near-immediate pressure communication in the upper half of the test section is observed. The pressure at ports P11 and P12 respond almost immediately to the advancing pressure pulse, while P7 and P8 in the transition zone inside the test cell follow soon after.

The solid lines in Figs. 17–20 correspond to model predictions with $\lambda = 0.2$ and $\ell = 0.575$, suggesting a permeability ratio of 1/25 between the bottom part cement and the solid mass above the top-of-cement. The choice of $\ell = 0.575$, which results in reasonable agreement between pressure measurements and model predictions, suggests the effective permeability variation to occur at approximately 5.4 m from the bottom of the section and that nearly all the pressure drop occurs in this bottom part of the section. As pointed out in the description of the test section above, surface re-logging indicated the transition from cement to "mud" to occur between 4.5 m and 5.8 m [15], agreeing well with the observed permeability variation in these tests. Finally, the equivalent micro-annulus of the cemented bottom part of the transition joint, which is measured to be approximately 30 μm, is within the range of effective wellbore permeabilities found in other wells from previous sustained casing pressure and vertical interference tests, as reported in Refs. [10,11].
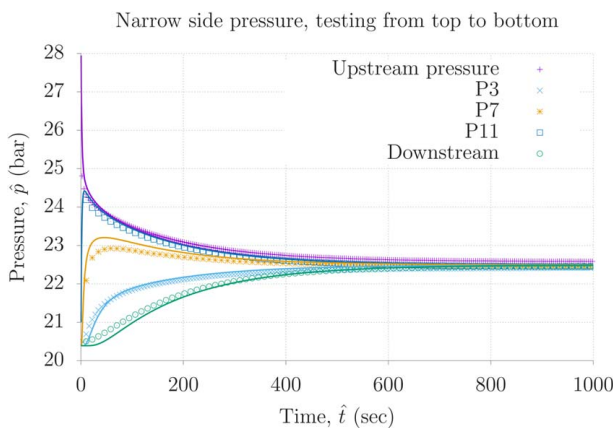

Fig. 20 The configuration is the same as in Fig. 18, but now in the reverse direction (the upstream reservoir connected to the top ("mud") part of the test section and the downstream reservoir to the bottom, cemented end)
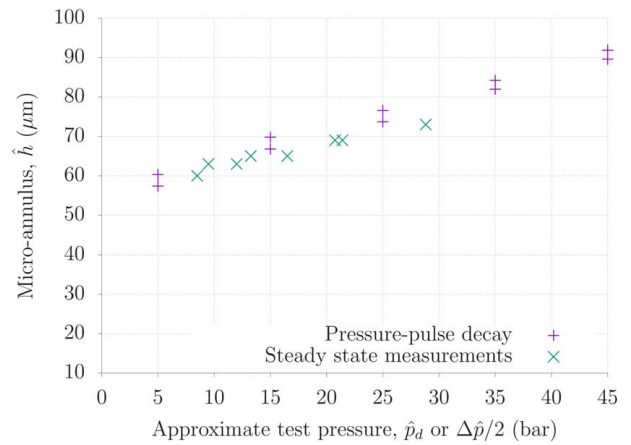

Fig. 21 Comparison of measured micro-annulus size for the PWC Jig when measuring with the steady-state method or the pressure-pulse-decay method

7 Discussion

In Fig. 21, a comparison of measured micro-annulus sizes for the PWC Jig is provided, showing values obtained with both the steady-state method and the transient pressure-pulse-decay method. As the effective micro-annulus size is sensitive to the applied test pressure, the values are plotted as function of either the initial downstream reservoir pressure, $\hat{p}_d$, or half the applied injection pressure in the case of steady-state measurements. For both samples and all tests reported here, an increase in effective permeability and equivalent micro-annulus gap size are found with increasing test pressures, both for the transient and the steady-state measurements. As indicated in Fig. 11, the increase in effective permeability can be linked to the elastic expansion of the test cell caused by the higher pressure. The simplistic interpretation is based on the assumption of a dominant seepage path along the outer casing and cement interface and that the pressure expands the casing radially. While this appears to be a reasonable approximation for the PWC Jig, where cement shrinkage during curing is a likely reason for the fairly high permeabilities, the transition joint shows seepage paths along both casing interfaces and through flaws in the cement, as visualized in Refs. [16,28]. In these more complex cases, the effective micro-annulus characterization is not necessarily a true description of the dimensions of the seepage paths. However, it remains a practical means of assessing the sealability of the annulus cement and comparing seepage measurements across different samples and at different pressures.

The uniform and heterogeneous permeability pressure diffusion models utilized to interpret pressure-pulse-decay measurements are based on the linear diffusion equation with pressure-independent material properties. The linear theory for transient pressure measurements is well developed and straight-forward to apply for measurement analyses. As initial conditions in the experiments reported above, a pressure pulse of approximately 10 bar has been used, which is of the same order of magnitude as the initial pressure in the test cell and the downstream reservoir. Although the choice of a significant pressure pulse can improve measurement accuracy, it could also introduce complicating nonlinear diffusion effects [29], as will be discussed below.

It is observed that the permeability or equivalent micro-annulus measurements for both the PWC Jig and the transition joint suggest an increasing value of permeability and an increasing effective micro-annulus size with increasing initial downstream test pressures. Consequently, in the case of a large initial pressure pulse, the pressure-variation in permeability may be non-negligible and have an effect on the diffusion through the test section. Pressure-dependent material properties lead to a pressure-dependence in the diffusion coefficient and also a quadratic term $\left(\partial \hat{p} / \partial \hat{x} \right)^2$ in the
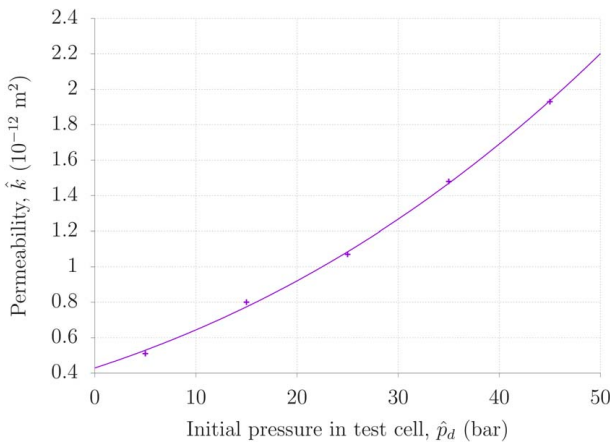
Fig. 22 Permeability variation with initial test cell and down-stream reservoir pressures

diffusion equation (3). The magnitude of the quadratic term will be proportional to the size of the pressure pulse, $\Delta \hat{p} = \hat{p}_u(0) - \hat{p}_d(0)$, and compressibility factors that describe the pressure-dependence of material properties, such as $\hat{c}_{\hat{k}} = (1/\hat{k})\partial\hat{k}/\partial\hat{p}$ for the permeability. While the quadratic pressure term can be eliminated through the Cole–Hopf transformation $p \rightarrow \ln(\beta p^*)/\beta$ [22,30], the pressure-dependent diffusion coefficient and boundary conditions complicate the solution of the diffusion equation when the pressure-dependence is not known in advance.

Consider in Fig. 22 the permeability measurements for the PWC Jig from Table 3 as function of the initial pressure in the test jig and the downstream reservoir. The solid line in the figure represents a curve fit to a single exponential $\hat{k}(\hat{p}) = \hat{k}_0 \exp(\hat{c}_{\hat{k}}\hat{p})$, where we find $\hat{c}_{\hat{k}} = 3 \times 10^{-7}$ 1/Pa, and $\hat{c}_{\hat{k}}\Delta\hat{p} = 0.3 \gg 0$ for these experiments. This would suggest that nonlinear effects could influence the experiments and interpretation. However, repeat tests with a smaller initial pressure difference between the reservoirs did not indicate systematic deviations from the above results. Furthermore, the permeability measurements from the experiments above avoided the early-time behavior where the pressure difference is large and utilize late-time measurements where the pressure difference across the test cells is of a few bars or less, and where there should be less spatial pressure-variation in the permeability. The quantitative agreement between measurements in both test cells and the heterogeneous permeability model suggests that the linear model is able to capture the dominant late-time diffusion effects in the experiments.

8 Summary and Conclusion

I have studied the permeability and equivalent micro-annulus in two full-scale cemented annulus test cells denoted PWC Jig and transition joint, where the latter originates from a 30 years old Norwegian North Sea production well that was abandoned in 2018. I have characterized the two test sections using a combination of transient pressure and steady-state seepage measurements, focusing primarily on the pressure-pulse-decay method and identification of permeability variations in the test cells. To this end, a transient model that predicts the pressure response through the system has been presented and fitted to experimental pressure measurements from the two reservoirs and from selected axial positions along the test cells. An important motivation for introducing the transient pressure-pulse-decay test protocol is to enable quick and reliable permeability measurement.

In conclusion, two independent test protocols are outlined and it is shown that they produce consistent measurements of permeability of full-scale cemented test sections. Overall, good quantitative agreement is found between pressure-pulse-decay measurements and comparable steady-state seepage tests on the same sections. Measured permeability variations are consistent with the

top-of-cement in one of the test cells and more competent bottom cement in the other. The permeabilities of the sections are sensitive to inner casing pressure and to the annular test pressure. These observations agree with previous work that found fracture-like character of migration paths behind casing. Finally, these results indicate that the transient test procedure can be used to more effectively characterize low-permeable annular cement where it is otherwise difficult to establish steady-state flow conditions. Transient pressure testing of less permeable sections than those studied here will be pursued as part of future work.

Conflict of Interest

There are no conflicts of interest.

Data Availability Statement

The authors attest that all data for this study are included in the paper.

References

[1] Bois, A.-P., Garnier, A., Rodot, F., Saint-Marc, J., and Aimard, N., 2011, "How to Prevent Loss of Zonal Isolation Through a Comprehensive Analysis of Microannulus Formation," SPE Drill. Complet., **26**(1), pp. 13–31.

[2] Patel, H., and Salehi, S., 2019, "Development of an Advanced Finite Element Model and Parametric Study to Evaluate Cement Sheath Barrier," ASME J. Energy Resour. Technol., **141**(9), p. 092902.

[3] Brufatto, C., Cochran, J., Conn, L., Power, D., El-Zeghaty, S., Fraboulet, B., Griffin, T., James, S., Munk, T., Justus, F., Levine, J., Montgomery, C., Murphy, D., Pfeiffer, J., Pornpoch, T., and Rishmani, L., 2003, "From Mud to Cement—Building Gas Wells," Oilfield Rev., **15**(3), pp. 62–76.

[4] Davies, R. J., Almond, S., Ward, R. S., Jackson, R. B., Adams, C., Worrall, F., Herringshaw, L. G., Gluyas, J. G., and Whitehead, M. A., 2014, "Oil and Gas Wells and Their Integrity: Implications for Shale and Unconventional Resource Exploitation," Mar. Pet. Geol., **56**(4), pp. 239–254.

[5] Nelson, E. B., and Guillot, D., 2006, Well Cementing, 2nd ed., Schlumberger, Sugar Land, TX.

[6] Duguid, A., Butsch, R., Carey, W. J., Celia, M., Chugunav, N., Gasda, S., Ramakrishnan, T. S., Stamp, V., and Wang, J., 2013, "Pre-Injection Baseline Data Collection to Establish Existing Wellbore Leakage Properties," Energy Procedia, **37**, pp. 5661–5672.

[7] Agbasimalo, N., and Radonjic, M., 2014, "Experimental Study of the Impact of Drilling Fluid Contamination on the Integrity of Cement-Formation Interface," ASME J. Energy Resour. Technol., **136**(4), p. 042908.

[8] Taleghani, A. D., and Klimenko, D., 2015, "An Analytical Solution for Microannulus Cracks Developed Around a Wellbore," ASME J. Energy Resour. Technol., **137**(6), p. 062901.

[9] Stormont, J. C., Garcia Fernandez, S., Taha, M. R., and Matteo, E. N., 2018, "Gas Flow Through Cement-Casing Microannuli Under Varying Stress Conditions," Geomech. Energy Environ., **13**(4), pp. 1–13.

[10] Gasda, S., Celia, M. A., Wang, J. Z., and Duguid, A., 2013, "Wellbore Permeability Estimates From Vertical Interferencetesting of Existing Wells," Energy Procedia, **37**(1), pp. 5673–5680.

[11] Checkai, D., Bryant, S., and Tao, Q., 2013, "Towards a Frequency Distribution of Effective Permeabilities of Leaky Wellbores," Energy Procedia, **37**, pp. 5653–5660.

[12] Crow, W., Carey, J. W., Gasda, S., Williams, B., and Celia, M., 2010, "Wellbore Integrity Analysis of a Natural CO_2 Producer," Int. J. Greenhouse Gas Control, **4**(2), pp. 186–197.

[13] Kang, M., Baik, E., Miller, A. R., Bandilla, K. W., and Celia, M. A., 2015, "Effective Permeabilities of Abandoned Oil and Gas Wells: Analysis of Data From Pennsylvania," Environ. Sci. Technol., **49**(7), pp. 4757–4764.

[14] Santos, L., and Taleghani, A. D., 2022, "On Quantitative Assessment of Effective Cement Bonding to Guarantee Wellbore Integrity," ASME J. Energy Resour. Technol., **144**(1), p. 013001.

[15] Obando Palacio, G., Gardner, D., Delabroy, L., and Govil, A., 2020, "An Evaluation of the Cement Sheath Quality of Casing Sections Recovered During a Well Abandonment Operation," IADC/SPE International Drilling Conference and Exhibition, Galveston, TX, Mar. 3–5, pp. 1–20, Paper No. IADC/SPE 199609.

[16] Skadsem, H. J., Gardner, D., Beltrán-Jiménez, K., Govil, A., Palacio, G. O., and Delabroy, L., 2021, "Study of Ultrasonic Logs and Seepage Potential on Sandwich Sections Retrieved From a North Sea Production Well," SPE Drill. Complet., pp. 1–15.

[17] Brace, W. F., Walsh, J. B., and Frangos, W. T., 1968, "Permeability of Granite Under High Pressure," J. Geophys. Res., 73(6), pp. 2225–2236.

[18] Hsieh, P. A., Tracy, J. V., Neuzil, C. E., Bredehoeft, J. D., and Silliman, S. E., 1981, "A Transient Laboratory Method for Determining the Hydraulic Properties of 'Tight' Rocks—I. Theory," Int. J. Rock Mech. Min. Sci. Geomech. Abstr., 18(3), pp. 245–252.

[19] Dicker, A. I., and Smits, R. M., 1988, "A Practical Approach for Determining Permeability From Laboratory Pressure-Pulse Decay Measurements," SPE International Meeting on Petroleum Engineering, pp. 1–8, Paper No. SPE 17578.

[20] Jones, S. C., 1997, "A Technique for Faster Pulse-Decay Permeability Measurements in Tight Rocks," SPE Form. Eval., 12(1), pp. 19–25.

[21] Haskett, S. E., Narahara, G. M., and Holditch, S. A., 1988, "A Method for Simultaneous Determination of Permeability and Porosity in Low-Permeability Cores," SPE Form. Eval., 3(3), pp. 651–658.

[22] Marshall, S. L., 2009, "Nonlinear Pressure Diffusion in Flow of Compressible Liquids Through Porous Media," Transp. Porous Med., 77(3), pp. 431–446.

[23] Hannon, M. J., Jr., 2016, "Alternative Approaches for Transient-Flow Laboratory-Scale Permeametry," Transp. Porous Med., 114(3), pp. 719–746.

[24] Han, G., Sun, L., Liu, Y., and Zhou, S., 2018, "Analysis Method of Pulse Decay Tests for Dual-Porosity Cores," J. Nat. Gas Sci. Eng., 59(2), pp. 274–286.

[25] Crank, J., 1975, The Mathematics of Diffusion, 2nd ed., Clarendon Press, Oxford, UK.

[26] Press, W. H., Teukolsky, S. A., Vetterling, W. T., and Flannery, B. P., 2001, Numerical Recipes in Fortran 77, 2nd ed., Cambridge University Press, Cambridge, UK.

[27] Stehfest, H., 1970, "Algorithm 368: Numerical Inversion of Laplace Transforms," Commun. ACM, 13(1), pp. 47–49.

[28] Skadsem, H. J., Gardner, D., Beltrán-Jiménez, K., Kragset, S., Delabroy, L., and Ruckert, F., 2020, "Fluid Migration Characterization of Cemented Sections Retrieved From a North Sea Production Well," IADC/SPE International Drilling Conference and Exhibition, Galveston, TX, Mar. 3–5, pp. 1–17, Paper No. IADC/SPE 199662.

[29] Walder, J., and Nur, A., 1986, "Permeability Measurement by the Pulse-Decay Method: Effects of Poroelastic Phenomena and Non-linear Pore Pressure Diffusion," Int. J. Rock Mech. Min. Sci. Geomech. Abstr., 23(3), pp. 225–232.

[30] Odeh, A. S., and Babu, D. K., 1988, "Comparison of Solutions of the Nonlinear and Linearized Diffusion Equations," SPE Reserv. Eng., 3(4), pp. 1202–1206.